Author(s): Tapio, Kosti; Kielar, Charlotte; Parikka, Johannes M.; Keller, Adrian; Järvinen, Heini; Fahmy, Karim; Toppari, J. Jussi

Title: Large-Scale Formation of DNA Origami Lattices on Silicon

Year: 2023

Version: Published version

Please cite the original version:

Tapio, K., Kielar, C., Parikka, J. M., Keller, A., Järvinen, H., Fahmy, K., & Toppari, J. J. (2023). Large-Scale Formation of DNA Origami Lattices on Silicon. Chemistry of Materials, 35(5), 1961-1971. https://doi.org/10.1021/acs.chemmater.2c03190

Large-Scale Formation of DNA Origami Lattices on Silicon

Kosti Tapio,*[,#] Charlotte Kielar,[#] Johannes M. Parikka, Adrian Keller, Heini Järvinen, Karim Fahmy, and J. Jussi Toppari*

ACCESS | ___ Metrics & More | ___ Article Recommendations | ___ Supporting Information

ABSTRACT: In recent years, hierarchical nanostructures have found applications in fields like diagnostics, medicine, nano-optics, and nano-electronics, especially in challenging applications like the creation of metasurfaces with unique optical properties. One of the promising materials to fabricate such nanostructures has been DNA due to its robust self-assembly properties and plethora of different functionalization schemes. Here, we demonstrate the assembly of a two-dimensional fishnet-type lattice on a silicon substrate using cross-shaped DNA origami as the building block, *i.e.*, tile. The effects of different environmental and structural factors are investigated under liquid atomic force microscopy (AFM) to optimize the lattice assembly. Furthermore, the arm-to-arm binding affinity of the tiles is analyzed, revealing preferential orientations. From the liquid AFM results, we develop a methodology to produce closely-spaced DNA origami lattices on silicon substrate, which allows further nanofabrication process steps, such as metallization. This formed polycrystalline lattice has high surface coverage and is extendable to the wafer scale with an average domain size of about a micrometer. Further studies are needed to increase the domain size toward a single-crystalline large-scale lattice.
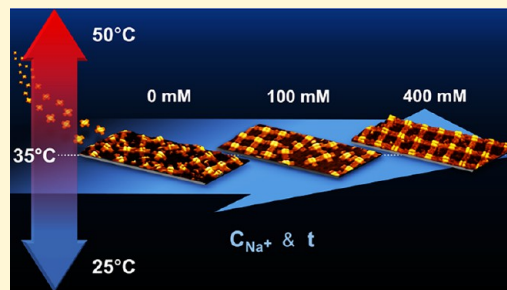
INTRODUCTION

In the modern era, the key innovations in different industrial fields are frequently based on nanoscale phenomena. Especially in the field of optics, applications such as superlenses can be realized by crafting highly ordered plasmonic nanostructures.[1−3] However, making such nanostructures with the current top-down fabrication processes requires precise, nanometer-scale spatial control and resolution, which are achievable only using the most sophisticated microfabrication methods like deep/extreme ultraviolet or electron beam lithography, which all have their limitations when it comes to throughput, cost, and fabrication time.[4] Meanwhile, bottom-up techniques to assemble hierarchical nanostructures have evolved rapidly owing to nanoscale materials like cellulose crystals, chitin, and graphene.[5−8] Yet, one of the most promising candidates has been DNA due to its robust self-assembly and plethora of different functionalization options.[9−11]

A particularly interesting method to fabricate hierarchical supramolecular structures is DNA origami[10] since it allows folding of arbitrarily shaped nanostructures that can be further designed to organize into larger entities via different interactions like DNA hybridization or blunt end stacking under certain user-defined conditions.[12,13] In the past, different kinds of DNA origami, like rectangles,[14,15] cross-shapes, the so-called Seeman tiles,[16,17] and triangles,[17−19] have been arranged into two-dimensional (2D) lattices. Also, 3D lattices[20,21] or assemblies like tubes and gears[22,23] have been realized, either in solution or on a surface.

Assembling large DNA origami lattices on surfaces creates new ways to craft metamaterial surfaces for nano-optics applications.[12,13] Especially, the recently introduced DNA-assisted lithography (DALI) enables direct transformation of the DNA origami shapes into metallic structures on different substrates.[24,25] This could offer a straightforward way to create plasmonic metasurfaces such as the fishnet-type metallic lattice,[26] which has unique properties like a negative refractive index.[3] One example of a self-assembled fishnet-type lattice has been achieved using the cross-shaped Seeman tile (ST) DNA origami. However, this has been realized only on a mica surface via direct formation of the lattice on the surface,[17] *i.e.*, surface-assisted assembly,[12,13] or with lattices formed within bulk solution and then deposited on mica.[16] To fully employ DALI or any other pattern transfer method[27] to obtain metasurfaces, the formation of the lattice needs to be extended to a silicon substrate, a feat that so far has not been fully realized.

Here, we first systematically investigate the main factors that influence the lattice formation of ST DNA origami on the silicon substrate during the deposition in liquid conditions, *i.e.*, ionic conditions of the buffer, temperature, and binding strength between the DNA origami. In addition, the influences

of minor structural changes of the ST DNA origami are also reported. These findings are then finally applied to demonstrate a methodology to obtain closely-spaced DNA origami lattices on the silicon substrate in the dry state. The obtained surface coverage of this kind of polycrystalline lattice with an average domain size of ∼850 nm is very high over large areas and extendable even up to the wafer scale, as has been already demonstrated on mica.[28] However, further studies are needed to increase the domain size toward a single-crystalline large-scale lattice. In the future, this concept can be used to fabricate metasurfaces using, *e.g.*, DALI.

■ EXPERIMENTAL SECTION

Folding and Purification of DNA Origami. The scaffold strand utilized in all the origami structures was M13mp18 (7249 nt) ordered from Tilibit (Tilibit Nanosystems GmbH, Friedenstraße 18, 81671 München, Germany). The staple strands (100 μM in water) for the twist-corrected (TC) and non-twist-corrected (NTC) Seeman tile (ST) DNA origami structures were purchased from Thermo Fisher Scientific (Waltham, Massachusetts, USA) and Integrated DNA Technologies (IDTDNA, 1710 Commercial Park, Coralville, Iowa 52241, USA), respectively. The staple mixes were prepared by mixing equal amounts of the core strands and necessary edge strands:[17] for the full and no blunt end design of TC-ST, either all the edge strands were added or removed. For the half blunt end design of TC-ST, the edge strands between helices 0−1, 2−3, 10−11, 15−16, 23−24, and 25−26 from both sides of the origami (see tables for the TC-ST tile from ref [17]) were removed from the staple mix. In NTC-ST, the sticky ends were replaced by blunt ends by removing the 5 nt long sticky end sequences from the edge staples.[16] The modified staples are listed in Table S1 (see tables for NTC-ST tile from ref [16]). The final concentration of a single staple in the staple mix varied slightly due to different amounts of staples needed for each design: full blunt end TC-ST ∼476 nM, half Blunt end TC-ST ∼505 nM, no blunt end TC-ST ∼538 nM, and NTC-ST ∼444 nM. Due to the excess number of staples over scaffold strands, these variations do not affect the folding.

The origamis were folded by mixing 80 μL of staple mix, 10 μL of a 100 nM scaffold strand, and 10 μL of 10× TAE + 150 mM MgCl$_2$ buffer. The solution was mixed and heated up in a FITX5-ABI Applied Biosystems thermocycler (Thermo Fisher Scientific) to 80 °C and cooled down to 20 °C in 16 min per 1 °C step (the total folding time was 16 h). Typically, at least three origami batches were prepared at once. The samples were purified using Amicon Ultra 100 kDa filters (Amicon Ultra): three batches of origami were pipetted into the same filter, and 200 μL of Millipore water was added. The sample was spinning in a Heraeus Megafuge 16 centrifuge (Thermo Fisher Scientific) for 5 min with a 9880 relative centrifugal force (rcf), and the flowthrough was discarded. Then, 450 μL of Millipore water was added and the spinning and the discarding of the flowthrough were repeated. The sample was spun three more times by adding 450 μL of Millipore water. Last, the sample was recovered by placing the filter tube upside down into a new filter tube and centrifuging it in 109 rcf for 2 min. The buffer was adjusted to 1× TAE + 12.5 mM MgCl$_2$, and the origami concentration was measured using a NanoDrop One C Microvolume UV−vis spectrophotometer (Thermo Fisher Scientific). A typical origami concentration was between 20 and 40 nM after the purification and the buffer adjustment.

Liquid Atomic Force Microscopy Imaging. AFM imaging in liquid was performed with an Asylum Cypher ES using a Biolever Mini BL-AC40TS-C2 cantilever (Olympus, Japan). The boron-doped single-crystal silicon wafers (⟨100⟩) were purchased from Si-Mat (Viktor-Frankl-Str. 20, 86916 Kaufering, Germany). Ammonium hydroxide (NH$_4$OH, 25%) was purchased from J.T. Baker, hydrogen peroxide (H$_2$O$_2$, 30%) from VWR chemicals, and sodium chloride (NaCl), magnesium dichloride hexahydrate (MgCl$_2$·6H$_2$O), and nickel dichloride hexahydrate (NiCl$_2$·6H$_2$O) from Merck. The silicon chips were cut from the wafer using a diamond cutter. They were then placed in a boiling acetone bath and scrubbed clean using cotton

sticks. Finally, the chips were sonicated in isopropanol (IPA) for 30 s and blown dry using N$_2$. The chips were then placed in boiling basic piranha solution (Millipore water:ammonium hydroxide:hydrogen peroxide = 5:1:1) for 15 min. After that, the chips were dipped and washed in two Millipore water baths and again dried using N$_2$.

For the liquid experiment at a constant temperature, 50 μL of the DNA origami solution (12 nM origami, 1× TAE buffer with 12.5 mM MgCl$_2$ and 0−150 mM NaCl) was pipetted onto a freshly treated silicon chip. An origami concentration of 12 nM was used since the lower tested concentrations of 8 and 10 nM did not cover the surface properly (data not shown). Finally, the cantilever was run into the sample droplet. The initial cantilever calibration was always performed at 25 °C, and the desired temperature was set only after moving the cantilever to the sample. A short readjustment of the detector signal was required after the temperature change just before starting the measurement to avoid drifting during the sample imaging. The calibration process requires a maximum of 5 min until the start of the measurement. In the set of measurement for temperature comparison, the origami samples were heated to either 25, 30, 35, 40, 45, or 50 °C, and to reach a steady state, the samples were allowed to settle for about 30 min at each temperature while continuously imaging them. After 30 min, the final image shown in Figure 3 was taken. Initially, the measurements at a constant temperature were carried out at 25 °C, but after the varied temperature experiments, we settled to 35 °C.

The sample chamber was heated at a rate of 1 °C/s. The images were recorded with scan sizes of 10 μm × 10 μm, 5 μm × 5 μm, or 3 μm × 3 μm, resolutions of 1024 px × 1024 px or 512 px × 512 px, and with scan rates of 4.88 and 1 Hz. The acquisition time per image was between 1.5 and 2 min, and thus, the deposition times have ±1 image or ±2 min error margin. AFM images measured in liquid were generated using Gwyddion[29] 2.55 and then combined into videos using the Image J program.

Lattice Formation in the Environmental Chamber Experiments. A Bruker Dimension Icon atomic force microscope (Bruker Corporation, 40 Manning Road, Billerica, MA 01821, USA) equipped with ScanAsyst air tips (the nominal radius = 2 nm) was used to characterize the lattice surface. The silicon chips were prepared similarly as in the liquid AFM measurements. After the hydrophilic treatment, the chip was dried and placed inside a 3 cm plastic Petri dish. The origami sample (stock concentration, 20−60 nM) was prepared by mixing the origami solution with 1× TAE, 12.5 mM MgCl$_2$ and 1× TAE, 12.5 mM MgCl$_2$, 3 M NaCl so that the end origami and sodium concentrations were appropriate. The total sample volume deposited on a 7 mm × 7 mm silicon chip was 20 μL. The Na$^+$ containing buffer was added last into the mixture, and the solution was immediately injected to the silicon chip. The Petri dish was sealed using a parafilm and placed inside the environmental chamber (Model WK3-180/40 by Weiss, Greizer Straße 41−4935447 Reiskirchen/Germany), which was already equilibrated to the desired temperature. The sample was kept inside for the planned deposition time, after which it was taken out, and 5 μL of 100 mM NiCl$_2$ was added to the 20 μL origami solution. The Petri dish and the sample were gently shaken and left to incubate for 30 s. The chip was taken out, and 100 μL of Millipore water was run through it three times while keeping the chip roughly in a 45° angle. Finally, the sample was dried using N$_2$ and imaged in AFM in air.

Analysis of the Lattice Quality. 2D fast Fourier transforms (FFTs) of the AFM images were calculated using Gwyddion.[29] The correlation lengths of the assembled DNA origami lattices were derived from the AFM images.[18] This was done by calculating the radial power spectral density functions (PSDs) of the images using Gwyddion[29] and fitting the first correlation peaks of the PSDs using Origin (OriginLab Corporation, One Roundhouse Plaza, Suite 303, Northampton, MA 01060, USA). The position and full width at half-maximum of the fitted correlation peak corresponded to the inverse lattice periodicity λ and the inverse correlation length ξ, respectively, the latter being a measure of the average size of single-crystalline domains in the lattices.
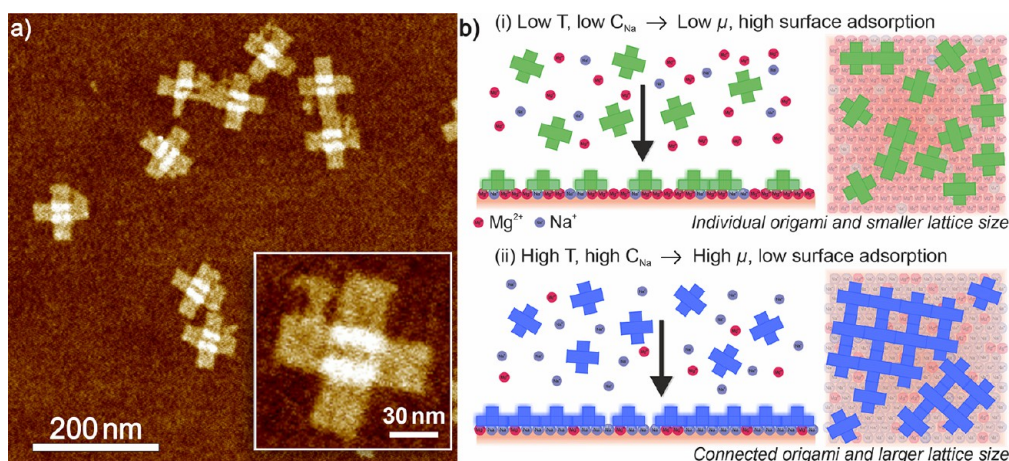
Figure 1. Twist-corrected Seeman tile (TC-ST) DNA origami. (a) AFM image of TC-STs on the silicon substrate. The inset shows individual TC-ST with the scaffold loop protruding from the structure.[17] Both panel (a) and the inset have a height scale of 4 nm. (b) Schematic view of TC-ST lattice formation on a silicon substrate. The surface adsorption of DNA origami is adjusted by temperature as well as by changing the concentration ratio between Mg^{2+} and Na^+ ions so that the magnesium concentration is kept fixed at 12.5 mM, and adjusting the Na^+ concentration (C_{Na}) changes the adsorption rate. (i) At low temperature and with relatively high surface adsorption ($C_{Na} \leq 100$ mM), surface mobility (μ) is low, and TC-STs attach directly and individually to the surface. (ii) At higher temperature and lower surface adsorption ($C_{Na} > 100$ mM), μ increases and attached TC-STs start to form larger lattices.
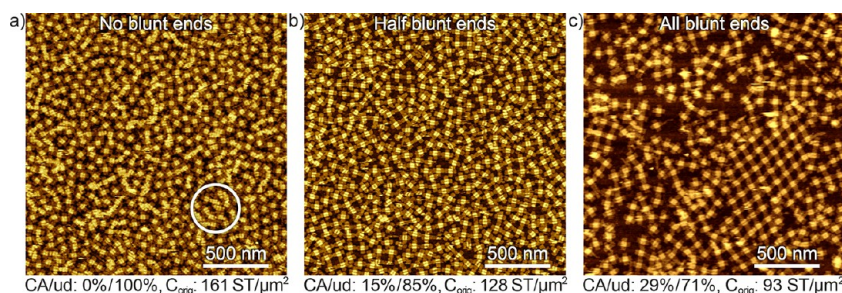

Figure 2. Effect of the number of blunt ends on the lattice formation at a temperature of 25 °C in 1× TAE with 12.5 mM $MgCl_2$ and 150 mM NaCl. The deposition times were 92 ± 2, 90 ± 2, and 87 ± 2 min in panels (a−c), respectively, and the origami concentration was 12 nM in all experiments. Image sizes are 2 μm × 2 μm with a height scale of 6 nm. (a) Deposition of TC-ST with no blunt ends. The white circle highlights an area where the TC-STs have close-packing symmetry. (b) Deposition of TC-ST with half (six) of the blunt ends. (c) Deposition of the TC-ST with all (12) the blunt ends. Statistics below show the fraction of connected arms (CA) against undefined/not-connected (ud) and surface density of the TC-ST origami (C_{orig}).

RESULTS AND DISCUSSION

DNA Origami and Lattice Design. Our fishnet-type lattice is formed using a blunt-ended twist-corrected version of the Seeman tile (TC-ST) DNA origami, which has a full 4-fold symmetry with respect to the structure and binding between DNA origami since any two arms can attach to each other.[17] Atomic force microscopy (AFM) images of separate TC-STs are shown in Figure 1a. Since the lattices formed in solution are limited in size due to shear forces and complications in the surface deposition,[12,16] we aimed for a lattice formation on a substrate, *i.e.*, surface-assisted assembly. For this reason, the chosen TC-ST can undergo blunt end stacking interactions between DNA origami, which allows oligomerization but does not lead to full lattice formation in solution.[17]

As a substrate, we use single-crystal silicon wafers, which form a native oxide layer on top under ambient conditions. The surface chemistry is thus governed rather by silicon oxide (SiO_2) than pure silicon (Si). Just before the deposition of the DNA origami, the Si substrate is treated with basic piranha solution, which deprotonates the terminal silanol groups, making the substrate negatively charged and thus hydrophilic, like the freshly cleaved mica surface (see the Supporting

Information for details). A schematic view of the origami deposition process is shown in Figure 1b. The surface deposition of TC-STs and the formation of the lattice are influenced by the distribution of surface charges, the concentration of monovalent and divalent cations in the solution, DNA origami concentration, incubation time, and temperature. The role of the cations is to facilitate TC-ST adsorption and lattice growth by reducing the repulsion between TC-STs so that the blunt end stacking can occur while enabling suitable adhesion to the substrate.

Based on wide literature,[12,13] increasing the surface mobility (μ) of the DNA origami should lead to improved lattice formation on a substrate and thus favor larger lattices. For the deposition, we used commonly utilized 1× TAE + 12.5 mM $MgCl_2$ (Mg^{2+}) buffer with varied concentrations (C_{Na}) of NaCl (Na^+). After injection, the hydrophilic negative surface is covered by both cations, and depending on the initial concentrations, the adsorption of TC-STs to the surface is either increased (case i, lower C_{Na}) or decreased (case ii, higher C_{Na}), as illustrated in Figure 1b. This directly affects μ since in the case of high surface affinity, the individual DNA origami structures stick more easily to the surface without
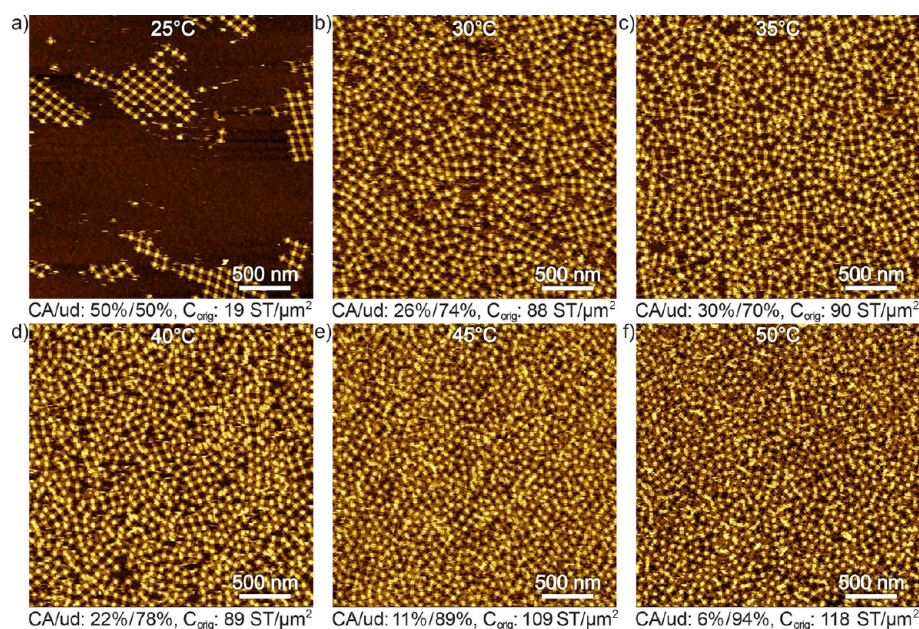
Figure 3. Effect of temperature on the lattice formation. The buffer was 1× TAE with 12.5 mM $MgCl_2$ and 150 mM NaCl. The deposition time was 30 ± 2 min, and the DNA origami concentration was 12 nM in all experiments. The image sizes are 2.8 μm × 2.8 μm with a height scale of 6 nm for all of the images. (a−f) Deposition of TC-ST at 25, 30, 35, 40, 45, and 50 °C, respectively. Statistics below show the fractions of CA and ud as well as the origami surface density (C_{orig}).

interacting with each other. In addition, we used elevated temperatures (T) to facilitate higher mobility to reduce the number of lattice defects and favor more robust lattice growth.

Liquid *In Situ* Investigations. We set out to test the effect of each of the above factors by employing *in situ* liquid AFM imaging during the incubation of DNA origami solution on a hydrophilic Si substrate in controlled conditions. The strongest contribution on the lattice formation should result from the interactions between the TC-STs, *i.e.*, the blunt end stacking. The strength of this interaction can be tuned by adjusting the number of blunt ends on each arm of the TC-ST. We tested the influence of this by varying the number of blunt ends from 0 per arm (no blunt ends) to 6 per arm (half blunt ends) and 12 per arm (all blunt ends). The TC-ST with no blunt ends was used as a control to evaluate the behavior when the blunt end interactions are too weak to affect the system, *e.g.*, when the temperature is too high, or the salt concentrations are not optimal.

We selected the initial deposition conditions based on the previously established results[17] (see the Experimental Section for details). The DNA origami concentration was adjusted so that the deposition process could be tracked in a reasonable timeframe from the beginning to the end. As an example, Video S1 shows the full time-course of *in situ* AFM liquid imaging for deposition of TC-STs with half blunt ends, while the results for all the TC-ST types are shown in Figure 2 after about 90 min of deposition. It is evident that increasing the number of blunt ends leads to more interconnected TC-STs, *i.e.*, higher fraction of connected arms (CA) and a larger degree of lattice formation (see the Supporting Information and Figure S1 for more information). If the number of blunt ends is halved, then the origami surface density (C_{orig}) is increased, but only small crystal domains were observed, resulting in lower CA (see Figure 2b and Figure S2). When the blunt ends are totally removed, CA drops to zero and TC-STs are filling the surface with a much higher density than what is expected

for the perfectly formed fishnet lattice, *i.e.*, 120 $ST/\mu m^2$. Even though some degree of close packing geometry is observed (the white circle in Figure 2a), the surface has still holes or openings.

We continued with the full blunt-ended TC-ST and tested the effect of the temperature by heating up the origami sample to either 25, 30, 35, 40, 45, or 50 °C. At each temperature, we waited until the steady state was reached (∼30 min) before taking the final image, as shown in Figure 3 (for the whole time-course of the temperature experiment, see Videos S2−S7 and Figure S3 in the Supporting Information). As can be seen in Figure 3a−c, the temperature initially has a positive effect on the lattice formation with increasing surface density (19−90 $ST/\mu m^2$) and amount of CA, most possibly due to increased μ and thus the increased diffusion of TC-ST on the surface. The ostensibly higher fraction of CA in Figure 3a is just due to too low surface coverage. However, when the temperature is increased beyond 35 °C (Figure 3d−f), it has a counterproductive effect leading to the DNA origami partly overlapping each other and forming closely packed structures like in Figure 2a. This is shown as the further increase in the surface density (from 89 to 118 $ST/\mu m^2$), while the fraction of CA decreases from 22 to 6%. In this case, the increased mobility most probably overcomes the blunt end interaction, which is relatively weak.[30] Therefore, the optimal temperature for the lattice formation seems to be around 35 °C, which was chosen for the further experiments.

The effect of Na^+ was tested by increasing the NaCl concentration from 0 to 150 mM (see Figure 4 and Figure S4 and Videos S8−S11). Since divalent cations like Mg^{2+} are more efficient in attaching the negatively charged DNA origami to the surface, they lead to decreased mobility and more random and disorganized deposition, as visible in Figure 4a,b. The replacement of Mg^{2+} by Na^+ at the surface leads to lower surface adsorption, which favors more interconnected structures, *i.e.*, higher CA, as seen in Figure 4c,d. Lower
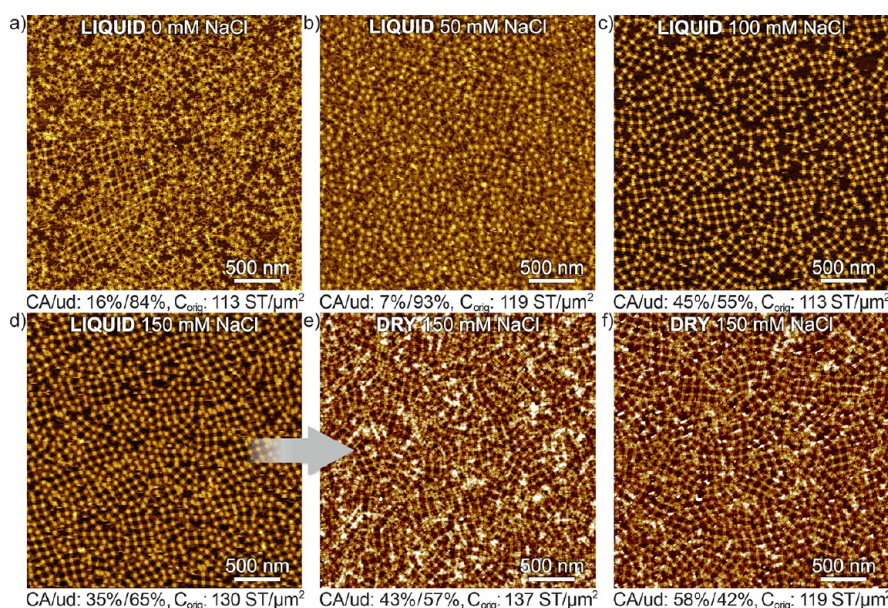
Figure 4. Effect of Na^+ on the lattice formation. (a−d) Deposition of TC-ST in 1× TAE with 12.5 mM $MgCl_2$ and 0, 50, 100, and 150 mM NaCl concentrations, respectively. The deposition times were 70 ± 2, 61 ± 2, 65 ± 2, and 184 ± 2 min in panels (a−d), respectively. The DNA origami concentration was 12 nM in each sample. (e, f) Deposition of TC-ST within an environmental chamber in 1× TAE with 12.5 mM $MgCl_2$ and 150 mM NaCl concentration. The samples are dried right after the brief Ni^{2+} treatment. The origami concentrations were 12 nM in panel (e) and 10 nM in panel (f). The image sizes are all 3 μm × 3 μm and have a height scale of 6 nm for panels (a−d), 4 nm for panel (e), and 4.5 nm for panel (f). Statistics below show the fractions of CA and ud as well as C_{orig}.

surface adhesion is also manifested by the longer deposition times needed to obtain the same surface coverage with higher Na^+ concentrations (see Figure S4). Thus, increasing the Na^+ concentration to 150 mM or above seems to have a positive effect on the lattice growth.

Finally, we tested the effect of structurally different versions of ST design. In literature, there are two versions of ST: twist-corrected (TC-)ST[17] and non-twist corrected (NTC-)ST.[16] All the previous experiments utilized the twist-corrected version, which has been shown to undergo surface-assisted assembly on mica.[17] However, formation of 2D lattices using other NTC-DNA origami designs like the Rothemund triangle (RT) has usually shown high surface mobility of the NTC-DNA origami.[31] To assess the performance of the NTC-ST to the TC-ST, we folded the blunt-ended version of the NTC-ST DNA origami from ref 16, where the sticky ends were removed from the arms (see the list of edge staples in Table S1), deposited them using the most promising parameters, i.e., 1× TAE with 12.5 mM $MgCl_2$ and 150 mM NaCl, and a DNA origami concentration of 12 nM, and tested the temperature dependence of NTC-ST lattice formation similarly, as shown in Figure 3. The results are shown in Figures S2 and S5−S7 and Videos S12−S15. Interestingly, the NTC-ST behaves in a completely different way than the TC-ST and only formed small, linear chains on silicon like those in Figures S5a−S7 and Video S15, and increasing the temperature only led to a higher surface diffusion rate. Based on previous CANDO simulations of this structure,[32] as well as similar observations on the effect of the origami twist on lattice formation,[14,33] we assume that this results from the highly deformed shape of the NTC-ST leading to non-flat adsorption with two opposing arms pointing away from the surface so that the blunt end stacking in this direction is no longer possible. Such behavior is in any case counter-productive for the 2D lattice formation, and so,

we opted to use the TC-ST structure in the following experiments.

To summarize the liquid AFM experiments, a temperature of 35 °C, the fully blunt-ended, twist-corrected design with a Mg^{2+} concentration of 12.5 mM, and a Na^+ concentration of at least 150 mM seem best to favor 2D lattice growth on a Si substrate, which is manifested as the increased fraction of CA and higher C_{orig}. The summary of the results of the liquid experiments is shown as a schematic table in Figure S8. In addition, by comparing our figures and especially videos on TC-ST DNA origami deposition with varying temperature, Na^+ concentration, and design, with the previous work on mica,[9,12] it seems that at least under the tested conditions, the surface mobility of the TC/NTC-ST origami is lower on the silicon substrate than on mica. To further demonstrate this, we conducted similar measurements, as shown in Figure 4d, but on a mica surface (see Video S16), where a higher surface mobility and larger lattices can be observed. In general, muscovite mica is a layered crystal consisting of negatively charged aluminosilicate sheets that are electrostatically stacked on top of each other via intermediate layers of K^+ ions.[34] In aqueous solution, the topmost K^+ ions desorb and leave a negatively charged surface behind. Since this mechanism is independent of pH, mica surfaces have a constant zeta potential of about −100 mV at pH values above 5.[35] The surface charge of SiO_2 surfaces, on the other hand, is caused by the deprotonation of terminal silanol groups, resulting in a strongly pH-dependent zeta potential that for most pH values is only about half that of mica.[36] Therefore, DNA origami adsorption on SiO_2 surfaces depends greatly on the deposition and surface conditions and needs to be tested more thoroughly for a proper conclusion.

Transfer to the Dry State. We used the above condition as a starting point to extend the protocol for fishnet TC-ST lattices on Si substrates up to the wafer scale, which in
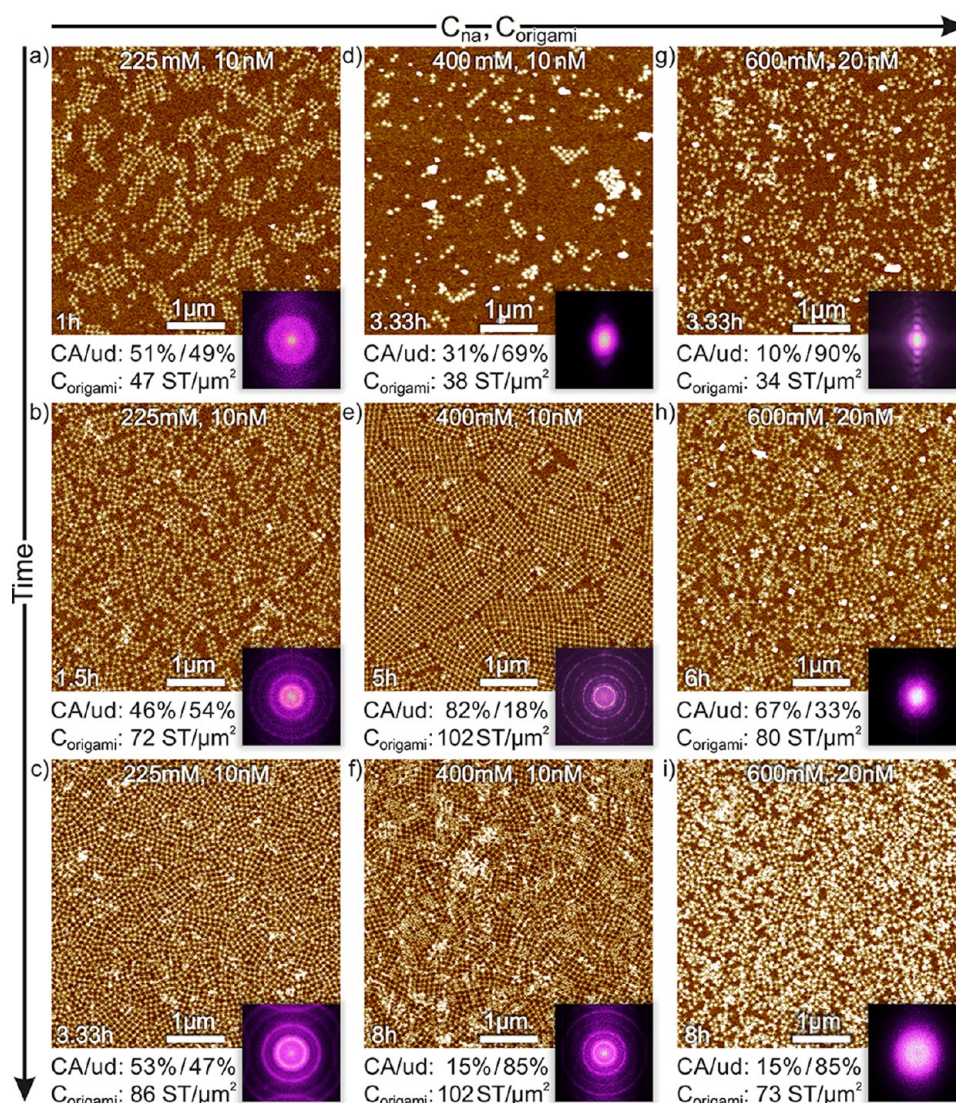
Figure 5. Formation of 2D TC-ST fishnet lattices on the Si substrate in the dry state using an environmental chamber. The surface coverage or density of the origami ($C_{origami}$) and the fraction of the connected arm (CA) and undefined arms (ud) are shown below each image. (a–i) AFM images of the TC-ST lattice formed in different buffer conditions and with different deposition times and DNA origami concentrations. The time dependency is displayed on the vertical axis, and the combined dependency on the DNA origami and Na^+ concentrations is shown in the horizontal axis. The incubation time is shown in the lower left corner, and the Na^+ and DNA origami concentrations are displayed on the top. The inset images show the fast Fourier transforms of the corresponding AFM images. The height scales are 4.5 nm for panel (a), 5 nm for panels (b–e), 4 nm for panel (f), 6 nm for panel (g), 5.5 nm for panel (h), and 6.5 nm for panel (i).

combination with DALI would enable us to produce large-scale metasurfaces. An important step still missing is the transfer from the liquid to the dry state since the imaging has been done so far in liquid, and further processing will require dried samples. Because *in situ* imaging is no longer needed, we can use an environmental chamber to control the temperature, which allows the processing of samples up to wafer size in a repeatable manner. However, although the larger lattices, *e.g.*, in Video S11, seem to attach to the Si substrate, TC-STs are still not firmly adsorbed and can easily be washed away, as shown in Figure S9a. Therefore, an additional adhesive element is required to fix them to the silicon substrate before washing and drying. Ni^{2+} is often employed as an adhesive material since it interacts with both the DNA backbone and the bases and is a widely used and established method to fix DNA to mica.[37,38] However, Ni^{2+} causes aggregation, so this step is very brief and done only at the very end. When the Ni^{2+}

treatment was employed, most of the origami stayed on the surface after drying (see Figure S9b). Thus, we opted to use the Ni^{2+} treatment in all the further dry state experiments below.

The starting point for the deposition within an environmental chamber was the most optimal result obtained with the incubation during the *in situ* imaging by liquid AFM using 1× TAE with 12.5 mM $MgCl_2$, 150 mM NaCl, and 12 nM origami, a temperature of 35 °C, and deposition time of 3 h. The result is shown in Figure 4e, which reveals approximately as good CA as in the liquid experiment, but partial formation of multilayer structures yields in total poorer quality of the lattice than in liquid. The reason is most probably the incorporated Ni^{2+} treatment, which fixes DNA origami to the surface more strongly, thus filling the surface too much, *i.e.*, density is higher than for the ideal lattice (137 ST/μm^2 > 120 ST/μm^2). Therefore, we lowered the concentration of DNA

origami from 12 to 10 nM, which resulted in a better-quality lattice, as shown in Figure 4f, *i.e.*, highest CA = 58% and almost an ideal surface density of 119 ST/μm^2. Thus, we used a 10 nM DNA origami concentration in the following experiments.

Yet, because the optimal Na$^+$ concentration from the liquid *in situ* studies was the highest one tested, the effect of it on the lattice formation was tested further by increasing the concentration even more from 150 up to 600 mM. However, the previously used incubation times (90−180 min) were not long enough to reach the steady state for the higher Na$^+$ concentrations and we needed to extend it, which was not possible in the liquid AFM due to evaporation. A higher Na$^+$ concentration of 400 mM results in better lattice formation, with the individual origami surface coverage or density (102 ST/μm^2 and 82% connected arms) and the size of the single-crystalline domains increasing after adjusting the deposition time to 5 h, as shown in Figure 5e. Similar results were observed on the mica surface.[17] An overly long incubation, however, leads to the deposition of multilayers, as seen in Figure 5f (400 mM Na$^+$, 10 nM, and 8 h). In general, we observed that to recover the surface coverage and lattice quality for the increased Na$^+$ concentration, we needed to either increase the DNA origami concentration, the incubation time, or both. Thus, to reduce the deposition time, a higher DNA origami concentration of 20 nM was tested while keeping the other conditions the same. This led to a similar-quality lattice (81 ST/μm^2 and CA 92%), as shown in Figure 5e, already within 3.33 h of incubation time, as shown in Figure S10a, but only with slightly stronger salt crystal deposition.

The Na$^+$ concentration was even further increased to 600 mM (Figure 5g−i), where the 20 nM DNA origami concentration was maintained, but the deposition time was varied from 3.33 to 8 h. All deposition times resulted in poorer quality lattices with the surface coverage varying between 34 and 80 ST/μm^2, fraction of the connected arms between 10 and 67%, and more salt crystals left on the surface. Most probably, a proper lattice formation would require a much longer time than 8 h. Since we could speed up the process by increasing the DNA origami concentration, the TC-ST deposition was carried out using the 600 mM NaCl and 30 nM DNA origami concentration while keeping the other parameters the same. This did not result in the improvement of the quality of the lattice (44 ST/μm^2 and CA 31%) within a 5 h deposition time. Although, it should be noted that there were more salt crystals left on the surface, which made estimating the amount of origami on the surface challenging (see Figure S10b).

The above observations suggest that increasing the Na$^+$ concentration even further would most probably lead into more salt crystal deposition and would require even higher DNA origami concentration and/or even longer deposition times. Therefore, we concluded that the 400 mM Na$^+$ concentration with 5 h of deposition time resulted in the highest quality lattice (82% connected arms and 102 ST/μm^2). For reassurance, we also tested the deposition at 25 and 45 °C for 400 mM Na$^+$ (Figure S11) as controls. They yielded either too low (26 ST/μm^2) or too high (257 ST/μm^2) coverages, respectively, ensuring the previous choice of 35 °C as the deposition temperature. These findings of the lattice formation on the silicon substrate using the environmental chamber are summarized in Table 1 and in Figure 5, which illuminates the dependency of the deposition protocol on the main parameters.

Table 1. Effect of Different Deposition Parameters on the Lattice Formation (LF) Observed after Drying the Sample[a]

T (°C)	C$_{origami}$ (nM)	C$_{Na}$ (mM)	t (h)	LF	Figure
35	12	150	3	+	4e
			3	−	4f
	10	225	1	✘	5a
			1.5	✘	5b
			3.33	−	5c
		400	3.33	✘	5d
			5	✔	5e
			8	+	5f
			3.33	✔	S9a
	20	400	3.33	✘	5g
		600	6	✘	5h
			8	✘	5i
	30	600	5	+	S9b

[a]Each row corresponds to a different deposition condition. The plus symbol, minus symbol, cross mark, and check mark represent either a case of multilayer, bad LF, no LF, or optimal LF, respectively.

To estimate further the quality of the lattices, we calculated the fast Fourier transforms (FFTs) of the AFM images. The insets in Figure 5 show the FFT of the corresponding AFM image. The FFTs of the images in the first row and the last column are dominated by noise and show only very faint correlation rings, which can be attributed to low surface coverage and/or poor lattice quality due to too short deposition time and too high Na$^+$ concentration, respectively. In the FFTs of the rest of the images, clear rings are visible due to the periodicity of the formed lattice. The rings are most pronounced in the middle (Figure 5e) image, which clearly shows sharp rings due to the distinct periodicity of the lattice. However, despite the lattice being of tetragonal symmetry, the rings are perfectly circular. This can be attributed to the fact that the single-crystalline domains display a high degree of order and barely any defects but are well separated from each other so that the crystal orientations are almost completely unaffected by that of neighboring domains. In this sense, the lattices rather represent 2D equivalents of powders instead of polycrystalline lattices in which grain boundaries are characterized by a high density of crystalline defects. Nevertheless, the FFT in Figure 5e shows a large number of concentric rings, consistent with higher order correlation peaks indicative of high lattice order. Closer inspection of the FFT further reveals pronounced intensity fluctuations in these rings at arbitrary angles as well as secondary features in the space between the inner rings. Such complex intensity fluctuations and secondary features have been observed also for other

highly ordered DNA origami lattices on mica surfaces and were shown to originate from the complex shapes of the DNA origami monomers.[18] Figure S12 shows extra FFT images of the TC-ST samples fabricated with the same best procedure used to obtain the results in Figure 5e. Note that this situation is markedly different from DNA origami lattices based on Rothemund triangles that do not rely on blunt end stacking and show overall hexagonal symmetry also in their FFTs.[18,31]

The periodicities and average domain sizes of the assembled lattices were estimated based on their correlation lengths calculated from the radial power spectral density (PSD) functions. For 400 mM NaCl, 10 nM TC-ST, and 5 h, an average periodicity of $\lambda = 91.1 \pm 0.1$ nm and a correlation length of $\xi = 850.1 \pm 4.6$ nm were obtained, resulting in a relative correlation length of $\xi/\lambda = 9.3 \pm 0.5$. This value is much higher than, e.g., that of the lattice in Figure 5c, which has a relative correlation length of only 4.9 ± 0.1. For different identically prepared samples equivalent to that shown in Figure 5e, the relative correlation length varied between 7.2 and 12.4. Figure S13 presents the results of the PSD analyses for all the analyzed samples. The results are also presented as numbers in Table S2.

Details of Blunt End Stacking. One fascinating observation is that the TC-ST DNA origami tends to favor a certain orientation within the crystals, as seen in Figures 2–4 and Figure S16: the two bars in the middle of the TC-ST are mostly oriented in the same direction. Therefore, as a starting point, we analyzed the binding between different arms from the liquid AFM data in Figure 4. Although it is possible to assign the arms to A1, A2, A3, and A4 based on the two bars and the position of the scaffold loop (see Figures S14–S16), the loop is not visible in the liquid imaging and thus the arms are assigned only as B1 and B2 based on the orientation of the two bars. The results are shown in Figure S15. In the case of no Na$^+$, B2–B2 binding is favored, while with 50 mM Na$^+$, there are a lot of unbound arms and poor-quality lattices. By increasing the Na$^+$ concentration, the lattices get better and the preference changes to B1–B1 binding, after which the amount of B1–B1 and B2–B2 bonds equalizes. We also analyzed the time dependency of binding affinity of the sample in Figure 4c (see Figure S17), where the observed initial (first 10 min) drop in both preferred bindings, B1–B1 and B2–B2, can be addressed to a frequent landing of new origami, which results in many partially imaged structures, thus raising the number of undefined (ud) bindings. Since the number of origami is low at the beginning, this induces a drop in the fraction of preferred bindings. This drop is, however, soon raised when the surface is filled. After that, attaching/detaching is slower and B1–B1 and B2–B2 bindings have continuously a high fraction while the weaker B1–B2 binding keeps fluctuating together with ud. After about 30 min, the lattice had reached steady state configuration.

To understand the preferential binding further, we analyzed several similar dry state samples like the one in Figure 5e (see Figure S18), where we can identify the scaffold loop, to more fundamentally deduce the arm specific binding preferences. The assignment and composition of the ST arms are shown in Figures S19 and S20, and the results of the counting are shown in Figure 6 as fractions, which are directly related to the binding affinity of each configuration. Interestingly, the arms have mostly a preference to bind to themselves (A1–A1, A2–A2, A3–A3, and A4–A4), although A1–A1 is lower than A1–A2 and there are a lot of cross bindings as well. When
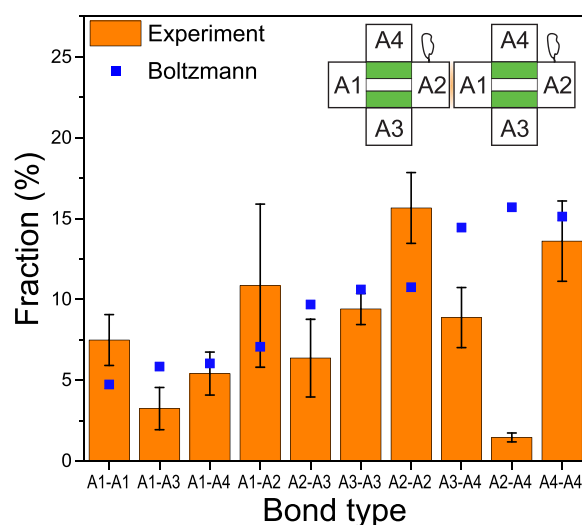

Figure 6. Analysis of different arm-to-arm blunt end binding configurations of STs in the environmental chamber experiments. The buffer condition was 1× TAE with 12.5 mM MgCl$_2$ and 400 mM NaCl, the temperature was 35 °C, and the incubation time was 5 h. As an example, the configuration A1–A2 is highlighted in the top right corner. The orange bars represent the fraction of the different configurations, and the blue dots are the fitted Boltzmann distribution P_{X-Y} calculated from the theoretical stacking energy (dG_{X-Y}) between the arms X and Y.

comparing the binding preference of the 400 mM NaCl dry sample to the liquid measurements of 150 nm NaCl, the binding goes from B1–B1 preference to more bidirectional, and the lattices grow equally in both directions (see Figure S15). Additionally, only certain combinations were preferred and primarily only 10 different arm-to-arm configurations exist, as shown in Figure S19. The common factor in all these cases is that the running direction of both DNA strands is preserved when transitioning from one origami to another, which is reasonable since the bound state resembles then a natural seamless DNA helix.

The observed specificity is only partially explained by the preservation of the running direction, and thus, we assessed the binding affinity between the arms in the configurations seen in Figure S19. Based on the previous work on the blunt end binding affinities,[39] we calculated the theoretical stacking energy per mol (dG_{X-Y}) for all the arm-to-arm compositions, $X-Y$. From this, we obtained the corresponding Boltzmann probability factors $p_{X-Y}(dG_{X-Y}, T) = \exp\left[-dG_{X-Y}/(N_A k_B T)\right]$, where the stacking energies were normalized by the Avogadro number, N_A. For details, see the Supporting Information, Figure S20 and Table S8. The Boltzmann distribution of different binding configurations P_{X-Y} based on p_{X-Y} is shown in Figure 6 together with the experimental data. It overall fits the data; however, the self-binding events like A1–A1 seem to be higher than predicted by the energy calculation and A2–A4 binding is much lower in experiments than in theory. The four lowest binding affinities (A1–A3, A1–A4, A2–A3, and A2–A4) require the flipping of one of the origami, which might be unpreferred due to, e.g., a surface bias and could explain the lower binding fraction. Among the non-flipped configurations, the self-binding seems to be preferential except in the case of A1, where the theoretical binding affinity is higher between A1 and A2 than A1 and A1. Unraveling this mystery would require further experiments, where one could tune more precisely the

interactions between the arms and see how the binding affinities change, which is out of scope of this study.

Nevertheless, two things can be noted though. First, the energies shown in Table S8 are calculated for the highest stacking energy, which is achieved by either fully bound arms or offset by one helix for all the 10 observed configurations. However, often, we observed that bound arms have even more offsets like in Figure 3 and Figures S18 and S19 (liquid and dry samples). Thus, naturally, the energies differ if the binding does not include all the blunt ends, but how many and which helices are contributing to the binding that is not clearly solvable based on the AFM data. Second, the binding affinities in ref 39 are measured in different conditions than in our case (either 500 mM NaCl or 20 mM MgCl$_2$), and as can be seen in Figure S6, the binding depends on the conditions of the surrounding medium. Last, one interesting note is that the preferential self-binding leads into highly oriented lattices, which would explain the observed results.

CONCLUSIONS

In summary, we have demonstrated how to assemble large-scale, polycrystalline lattices on Si substrates using Seeman tile DNA origami and investigated the conditions to reliably achieve large-scale lattices. The main factors influencing DNA origami deposition are the temperature, the Na$^+$ concentration, and the number of connecting blunt ends. Lower temperature leads into deposition of individual DNA origami with little interactions between them. When the temperature is increased, the DNA origami mobility increases, leading to larger lattices. However, when the temperature is raised too much, the DNA origami starts to partially stack to each other, overcoming the relatively weak blunt end stacking force. We observed that, initially, the higher Na$^+$ concentration leads to larger lattice domains, while for concentrations higher than 400 mM, the domain size does not increase anymore but is obscured by salt deposits. This is in line with previous observations on mica, where lattice assembly was favored at intermediate Na$^+$ concentrations.[18] Additionally, it was observed that the DNA origami structures inside the single-crystalline lattice domains were highly ordered and underwent directional binding. This is most probably because the blunt end interactions between the different arms of the ST are heterogeneous with binding between similar arms being more favorable. This concept could be expanded further in the future to fabricate fully customizable lattices, where one might control the orientation of the DNA origami inside the lattice. In combination with nanoparticles, this would allow the fabrication of highly oriented plasmonic metasurfaces. The currently obtained lattices can already be used for metallization by DALI[24] and turned into metasurfaces. However, for distinct optical applications, even larger single-crystalline lattice domains should be grown, which, however, will most likely require changes in the DNA origami design. One possibility could be inclusion of short protruding ssDNA extensions, which increase the binding affinity between STs. This has been employed in a previous study on a mica,[40] where larger domain sizes were achieved. This will be investigated in a future study as well.

ASSOCIATED CONTENT

Ⓢ Supporting Information

The Supporting Information is available free of charge at https://pubs.acs.org/doi/10.1021/acs.chemmater.2c03190.

Extra liquid AMF images and videos and a summary of the liquid imaging; AFM images of the nickel fixing and extra environmental chamber experiments as well as extra FFT images and statistics; the analysis of the binding affinities between the arms with corresponding AFM images and statistics, the calculations of the Boltzmann distribution for each arm binding, and the list of modified strands (PDF)

Video S1: Six-blunt TC-ST 150 mM NaCl 25 °C (AVI)
Video S2: TC-ST 150 mM NaCl 25 °C (AVI)
Video S3: TC-ST 150 mM NaCl 30 °C (AVI)
Video S4: TC-ST 150 mM NaCl 35 °C (AVI)
Video S5: TC-ST 150 mM NaCl 40 °C (AVI)
Video S6: TC-ST 150 mM NaCl 45 °C (AVI)
Video S7: TC-ST 150 mM NaCl 50 °C (AVI)
Video S8: TC-ST 0 mM NaCl 35 °C (AVI)
Video S9: TC-ST 50 mM NaCl 35 °C (AVI)
Video S10: TC-ST 100 mM NaCl 35 °C (AVI)
Video S11: TC-ST 150 mM NaCl 35 °C (AVI)
Video S12: NTC-ST 150 mM NaCl 25 °C (AVI)
Video S13: NTC-ST 150 mM NaCl 35 °C (AVI)
Video S14: NTC-ST 150 mM NaCl 25−45 °C (AVI)
Video S15: Stacking formation NTC-ST 150 mM NaCl 25 °C zoomed S12 (AVI)
Video S16: TC-ST 150 mM NaCl 35 °C mica (AVI)

AUTHOR INFORMATION

Corresponding Authors

Kosti Tapio — *Department of Physics and Nanoscience Center, University of Jyväskylä, 40014 Jyväskylä, Finland*; Present Address: Department of Neuroscience and Biomedical Engineering, Aalto University, 00076 Aalto, Finland; Email: kosti.t.o.tapio@jyu.fi

J. Jussi Toppari — *Department of Physics and Nanoscience Center, University of Jyväskylä, 40014 Jyväskylä, Finland*; ⓞ orcid.org/0000-0002-1698-5591; Email: j.jussi.toppari@jyu.fi

Authors

Charlotte Kielar — *Institute of Resource Ecology Helmholtz−Zentrum Dresden−Rossendorf (HZDR), 01328 Dresden, Germany*

Johannes M. Parikka — *Department of Physics and Nanoscience Center, University of Jyväskylä, 40014 Jyväskylä, Finland*

Adrian Keller — *Technical and Macromolecular Chemistry, Paderborn University, 33098 Paderborn, Germany*; ⓞ orcid.org/0000-0001-7139-3110

Heini Järvinen — *Department of Physics and Nanoscience Center, University of Jyväskylä, 40014 Jyväskylä, Finland*; Present Address: Microsoft Oy (Suomi), Keilalahdentie 2-4, 02150 Espoo, Finland

Karim Fahmy — *Institute of Resource Ecology Helmholtz−Zentrum Dresden−Rossendorf (HZDR), 01328 Dresden, Germany*; ⓞ orcid.org/0000-0002-8752-5824

Complete contact information is available at:
https://pubs.acs.org/10.1021/acs.chemmater.2c03190

Author Contributions

[#]K.T. and C.K. contributed equally. C.K. and K.T. performed the liquid AFM experiments and imaging. K.T., J.M.P., and H.J. prepared the environmental chamber samples and imaged

them. A.K. performed the FFT and PSD analysis. C.K. counted the binding affinities from AFM images, and K.T. calculated the theoretical Boltzmann distributions. J.J.T. conceived the research and coordinated it. J.J.T. and K.F. contributed to the result analysis, discussion, and interpretation. K.T. drafted the first version of the manuscript, while the final manuscript was written through contributions of all authors. All authors have given approval to the final version of the manuscript.

Notes

The authors declare no competing financial interest.

ABBREVIATIONS

ST, Seeman tile; DALI, DNA-assisted lithography; TC, twist-corrected; NTC, non-twist-corrected; rcf, relative centrifugal force; IPA, isopropanol; FFT, fast Fourier transforms; PSD, power spectral density; AFM, atomic force microscopy; RT, Rothemund triangle; LF, lattice formation

REFERENCES

(1) Pendry, J. B. Negative Refraction Makes a Perfect Lens. *Phys. Rev. Lett.* **2000**, *85*, 3966−3969.

(2) Wang, Z.; Cheng, F.; Winsor, T.; Liu, Y. Optical chiral metamaterials: a review of the fundamentals, fabrication methods and applications. *Nanotechnology* **2016**, *27*, No. 412001.

(3) Shalaev, V. M. Optical negative-index metamaterials. *Nat. Photonics* **2007**, *1*, 41−48.

(4) Kasani, S.; Curtin, K.; Wu, N. A review of 2D and 3D plasmonic nanostructure array patterns: fabrication, light management and sensing applications. *NANO* **2019**, *8*, 2065−2089.

(5) Geese, M.; Spengler, M. Cellulose nanocrystals in nano-architectonics − towards photonic functional materials. *Mol. Syst. Des. Eng.* **2019**, *4*, 29−48.

(6) Fan, Z.; Yan, J.; Zhi, L.; Zhang, Q.; Wei, T.; Feng, J.; Zhang, M.; Qian, W.; Wei, F. A three-dimensional carbon nanotube/graphene sandwich and its application as electrode in supercapacitors. *Adv. Mater.* **2010**, *22*, 3723−3728.

(7) Zhang, Q.; Wang, Y.; Zhang, B.; Zhao, K.; He, P.; Huang, B. 3D superelastic graphene aerogel-nanosheet hybrid hierarchical nano-structures as high-performance supercapacitor electrodes. *Carbon* **2018**, *127*, 449−458.

(8) Chandran, R.; Nowlin, K.; LaJeunesse, D. R. Nanosphere Lithography of Chitin and Chitosan with Colloidal and Self-Masking Patterning. *Polymer* **2018**, *10*, 218.

(9) Tapio, K.; Bald, I. The potential of DNA origami to build multifunctional materials. *Multifunct. Mater.* **2020**, *3*, No. 032001.

(10) Dey, S.; Fan, C.; Gothelf, K. V.; Li, J.; Lin, C.; Liu, L.; Liu, N.; Nijenhuis, M. A. D.; Saccà, B.; Simmel, F. C.; et al. DNA origami. *Nat. Rev. Methods Primers* **2021**, *1*, 13.

(11) Hong, F.; Zhang, F.; Liu, Y.; Yan, H. DNA Origami: Scaffolds for Creating Higher Order Structures. *Chem. Rev.* **2017**, *117*, 12584−12640.

(12) Parikka, J. M.; Sokolowska, K.; Markešević, N.; Toppari, J. J. Constructing Large 2D Lattices Out of DNA-Tiles. *Molecules* **2021**, *26*, 1502.

(13) Julin, S.; Keller, A.; Linko, V. Dynamics of DNA Origami Lattices. *Bioconjugate Chem.* **2023**, *34*, 18−29.

(14) Woo, S.; Rothemund, P. W. K. Self-assembly of two-dimensional DNA origami lattices using cation-controlled surface diffusion. *Nat. Commun.* **2014**, *5*, 4889.

(15) Tikhomirov, G.; Petersen, P.; Qian, L. Fractal assembly of micrometre-scale DNA origami arrays with arbitrary patterns. *Nature* **2017**, *552*, 67−71.

(16) Liu, W.; Zhong, H.; Wang, R.; Seeman, N. C. Crystalline Two-Dimensional DNA-Origami Arrays. *Angew. Chem., Int. Ed.* **2011**, *50*, 264−267.

(17) Rafat, A. A.; Pilzer, T.; Scheible, M. B.; Kostina, A.; Simmel, F. C. Surface-assisted large-scale ordering of DNA origami tiles. *Angew. Chem., Int. Ed.* **2014**, *53*, 7665−7668.

(18) Kielar, C.; Ramakrishnan, S.; Fricke, S.; Grundmeier, G.; Keller, A. Dynamics of DNA Origami Lattice Formation at Solid-Liquid Interfaces. *ACS Appl. Mater. Interfaces* **2018**, *10*, 44844−44853.

(19) Tikhomirov, G.; Petersen, P.; Qian, L. Triangular DNA Origami Tilings. *J. Am. Chem. Soc.* **2018**, *140*, 17361−17364.

(20) Zhang, T.; Hartl, C.; Frank, K.; Heuer-Jungemann, A.; Fischer, S.; Nickels, P. C.; Nickel, B.; Liedl, T. 3D DNA Origami Crystals. *Adv. Mater.* **2018**, *30*, 1800273.

(21) Gao, D.; Ma, N.; Yan, X.; Ji, M.; Zhu, J.-J.; Min, Q.; Tian, Y. Low-entropy lattices engineered through bridged DNA origami frames. *Chem. Sci.* **2021**, *13*, 283−289.

(22) Wagenbauer, K. F.; Sigl, C.; Dietz, H. Gigadalton-scale shape-programmable DNA assemblies. *Nature* **2017**, *552*, 78−83.

(23) Han, D.; Pal, S.; Nangreave, J.; Deng, Z.; Liu, Y.; Yao, H. DNA origami with complex curvatures in three-dimensional space. *Science* **2011**, *322*, 342−346.

(24) Shen, B.; Linko, V.; Tapio, K.; Pikker, S.; Lemma, T.; Gopinath, A.; Gothelf, K. V.; Kostiainen, M. A.; Toppari, J. J. Plasmonic nanostructures through DNA-assisted lithography. *Sci. Adv.* **2018**, *4*, No. eaap8978.

(25) Piskunen, P.; Shen, B.; Keller, A.; Toppari, J. J.; Kostiainen, M. A.; Linko, V. Biotemplated Lithography of Inorganic Nanostructures (BLIN) for Versatile Patterning of Functional Materials. *ACS Appl. Nano Mater.* **2021**, *4*, 529−538.

(26) Xiao, S.; Chettiar, U. K.; Kildishev, A. V.; Drachev, V. P.; Shalaev, V. M. Yellow-light negative-index metamaterials. *Opt. Lett.* **2009**, *34*, 3478−3480.

(27) Shen, J.; Sun, W.; Liu, D.; Schaus, T.; Yin, P. Three-dimensional nanolithography guided by DNA modular epitaxy. *Nat. Mater.* **2021**, *20*, 683−690.

(28) Xin, Y.; Shen, B.; Kostiainen, M. A.; Grundmeier, G.; Castro, M.; Linko, V.; Keller, A. Scaling Up DNA Origami Lattice Assembly. *Chem. − Eur. J.* **2021**, *27*, 8564−8571.

(29) Nečas, D.; Klapetek, P. Gwyddion: an open-source software for SPM data analysis. *Cent. Eur. J. Phys.* **2012**, *10*, 181−188.

(30) Wang, R.; Kuzuya, A.; Liu, W.; Seeman, N. C. Blunt-ended DNA stacking interactions in a 3-helix motif. *Chem. Commun.* **2010**, *46*, 4905−4907.

(31) Xin, Y.; Rivadeneira, S. M.; Grundmeier, G.; Castro, M.; Keller, A. Self-assembly of highly ordered DNA origami lattices at solid-liquid interfaces by controlling cation binding and exchange. *Nano Res.* **2020**, *13*, 3142−3150.

(32) Ramakrishnan, S.; Shen, B.; Kostiainen, M. A.; Grundmeier, G.; Keller, A.; Linko, V. Real-Time Observation of Superstructure-Dependent DNA Origami Digestion by DNase I Using High-Speed Atomic Force Microscopy. *ChemBioChem* **2019**, *20*, 2818−2823.

(33) Woo, S.; Rothemund, P. W. K. Programmable molecular recognition based on the geometry of DNA nanostructures. *Nat. Chem.* **2011**, *3*, 620−627.

(34) Keller, A.; Fritzsche, M.; Ogaki, R.; Bald, I.; Facsko, S.; Dong, M.; Kingshott, P.; Besenbacher, F. Tuning the hydrophobicity of mica surfaces by hyperthermal Ar ion irradiation. *J. Chem. Phys.* **2011**, *134*, 104705.

(35) Sides, P. J.; Faruqui, D.; Gellman, A. J. Dynamics of Charging of Muscovite Mica: Measurement and Modeling. *Langmuir* **2009**, *3*, 1475−1481.

(36) Barone, G.; Terenzi, A.; Lauria, A.; Almerico, A. M.; Leal, J. M.; Busto, N.; García, B. Zeta potential measurements of Ta2O5 and SiO2 thin films. *J. Colloid Interface Sci.* **2013**, *147*, 22−32.

(37) Barone, G.; Terenzi, A.; Lauria, A.; Almerico, A. M.; Leal, J. M.; Busto, N.; García, B. DNA-binding of nickel(II), copper(II) and zinc(II) complexes: Structure−affinity relationships. *Coord. Chem. Rev.* **2013**, *257*, 2848−2862.

(38) Liu, L.; Zheng, M.; Li, Z.; Li, Q.; Mao, C. Patterning Nanoparticles with DNA Molds. *ACS Appl. Mater. Interfaces* **2019**, *11*, 13853−13858.

(39) Kilchherr, F.; Wachauf, C.; Pelz, B.; Rief, M.; Zacharias, M.; Dietz, H. Single-molecule dissection of stacking forces in DNA. *Science* **2016**, *353*, aaf5508.

(40) Wang, P.; Gaitanaros, S.; Lee, S.; Bathe, M.; Shih, W. M.; Ke, Y. Programming Self-Assembly of DNA Origami Honeycomb Two-Dimensional Lattices and Plasmonic Metamaterials. *J. Am. Chem. Soc.* **2016**, *138*, 7733−7740.